ELSEVIER

Contents lists available at ScienceDirect

Thermochimica Acta

journal homepage: www.elsevier.com/locate/tca





Thermodynamic analysis of dehydration of K₂CO₃·1.5H₂O

Natalia Mazur^{a,b}, Henk Huinink^{a,b,*}, Bart Borm^a, Stefano Sansota^{a,c}, Hartmut Fischer^d, Olaf Adan^{a,b,d}

- ^a Eindhoven University of Technology, Den Dolech 2, Eindhoven, MB 5600, the Netherlands
- b Eindhoven Institute for Renewable Energy Systems, Eindhoven University of Technology, PO Box 513, Eindhoven, MB 5600, the Netherlands
- ^c CFM, University of the Basque Country, Paseo de Manuel Lardizabal, 5, Donostia-San Sebastian, Gipuzkoa 20018, Spain
- ^d TNO Materials Solutions, High Tech Campus 25, Eindhoven, AE 5656, the Netherlands

ARTICLE INFO

Keywords: Thermochemical energy storage Classical nucleation theory Transition state theory Dehydration of salts

ABSTRACT

This work studied the reversible dehydration of potassium carbonate sesquihydrate (K_2CO_3 ·1.5 H_2O). The study is based on isobaric and isothermal thermogravimetric measurements conducted at a broad range of vapour pressures and temperatures. By controlling both parameters, we examined the influence of both constraints on the reaction kinetics at a wide extent of supersaturations. We have evaluated our experimental findings by employing two thermodynamic theories, classical nucleation theory and transition state theory. By combining both approaches, we were able to establish that: (1) At low supersaturations in a region close to equilibrium, dehydration is limited by nucleation and growth of the anhydrous phase (2) At high supersaturations, dehydration reaches maximum rate and is controlled by the reaction speed. Furthermore, we show that the dehydration of K_2CO_3 ·1.5 H_2O is very sensitive to pressure-temperature conditions and that it does not possess universal activation energy.

1. Introduction

Dehydration properties of salt hydrates have been studied for decades, and with this, they have contributed significantly to the development of present theories of solid-solid phase transitions [1–3]. In recent years, the interest shifted from purely fundamental to application-oriented [4,5]. The interest in potassium carbonate sesquihydrate has followed similar development, where recently, it has been extensively studied as a thermochemical heat storage material [6–10]. Many other concepts and materials are available for heat storage applications [11] and the category of reversible reactions between salt and water vapour, is just one of the approaches under development [12].

The dehydration of K₂CO₃•1.5H₂O is a reversible process expressed

$$K_2CO_3 \cdot 1.5H_2O(s) \rightleftharpoons K_2CO_3(s) + 1.5H_2O(g)$$
 (Rx. 1)

On a macroscopic scale, the process is schematically represented in Fig. 1. During dehydration, a morphological change takes place in the crystal. When the water leaves the hydrate, a layer of solid anhydrous material forms on the surface. The thickness of that material will steadily increase with time till all material has dehydrated [13]. Water

vapour, generated during the reaction, must therefore diffuse through pores and cracks in the anhydrous salt to escape the solid [7].

Early studies on the dehydration of $K_2CO_3 \bullet 1.5H_2O$ have suggested the existence of monohydrate [14,15] or hemihydrate [16]; however, this was never fully confirmed [17,18]. The study by Stanish et al. [18] describes the dehydration process of $K_2CO_3 \bullet 1.5H_2O$ as a single step process of which the subsiding speed can be explained with the shrinking core model. This model describes reaction progress from outside of a particle towards its core, during which a shell of reacted material is formed, often causing diffusion issues. A similar model was used in the study by Gaeini et al. [8], who investigated the influence of temperature and vapour pressure on reaction kinetics far from equilibrium conditions.

In addition to decreasing dehydration speed with increasing conversion, Stanish et al. have observed extremely slow kinetics close to equilibrium conditions. A similar drastic drop in dehydration rate was observed by Sögütoglu et al. [19]. They have mapped out an area close to equilibrium conditions, dubbed the metastable zone (MSZ), where no instantaneous dehydration occurs. Fig. 2 illustrates the principle of this phenomenon, where the red line indicates the measured mass loss at 12 mbar vapour pressure when the temperature gradually increases from

^{*} Corresponding author at: Eindhoven University of Technology, Den Dolech 2, Eindhoven, MB 5600, the Netherlands. *E-mail address*: h.p.huinink@tue.nl (H. Huinink).

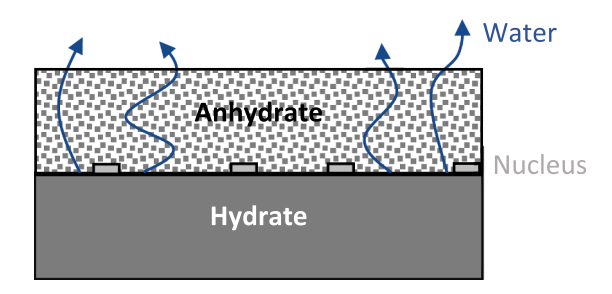


Fig. 1. Scheme of dehydration.

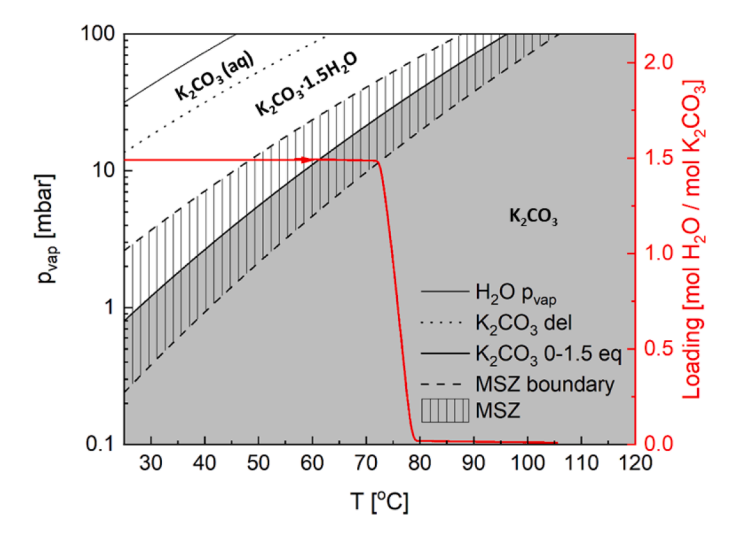


Fig. 2. K_2CO_3 pressure-temperature phase diagram adapted from Sögütoglu et al. [19]. p_{vap} is vapour pressure, and T is sample temperature. The red line shows the measured change in loading (right axis) at 12 mbar between 25-105 °C and at 0.3 °C/min heating rate.

25 to 105 °C. It shows a dormant period within the hatched area (MSZ), when temperature increases above the equilibrium line (thick black line) and when the dehydration starts (dashed line). This kind of hysteresis is not specific to potassium carbonate, as it has been observed in many other salt hydrates [20], and it is commonly associated with a nucleation barrier [21,22].

Considering all the previous observations, we have noticed that the dehydration behaviour of $K_2CO_3 \bullet 1.5H_2O$ is strongly dependent on the vapour pressure and its relationship to the equilibrium line. Therefore, depending on the reaction conditions, different phenomena can be observed. Those phenomena can lead to a series of limitations to the reaction progress, such as nucleation barrier, diffusion limitation or reaction limitation. Other salt hydrates [23–25] and other materials [13, 26,27] considered for heat storage have been subjected to thermodynamic analysis of their dehydration pathways to remove any ambiguities regarding phase transitions, elucidate limiting factors during the reaction and determine impact of reaction conditions on the reaction pathways. K_2CO_3 has not been subjected to such thorough study which might prove debilitating in further development of this material for practical applications.

The goal of this work is to reassess the dehydration behaviour of K_2CO_3 . Given the existence of two thermodynamically different zones, we aim to elucidate the influence of water vapour on the nature of dehydration at a wide range of conditions. Measurements are conducted at fixed isobaric-isothermal points within and outside of MSZ. The obtained data are evaluated from a thermodynamic point of view by taking driving force into account.

2. Theory of dehydration

The general dehydration reaction can be described as:

$$\begin{array}{c} k_1 \\ S \cdot b H_2 O(s) & \rightleftharpoons S \cdot a H_2 O(s) + (b-a) H_2 O(g) \\ k_2 \end{array} \tag{Rx.2} \label{eq:Rx.2}$$

where S is a salt unit, while b and a are the numbers of water molecules partaking in the reaction, and where b>a, and k_1 and k_2 are reaction rate constants for the forward and reverse reaction, respectively.

The Gibbs energy for the reaction, ΔG_r^0 [J/mol], is given as:

$$\Delta G_r^o = -RT ln \left(\frac{p}{p^o}\right) = \Delta H_r^o - T \Delta S_r^o \tag{1}$$

where R is the gas constant [8.3145 J/K mol], T [K] is the absolute temperature, p [mbar] is the vapour partial pressure, p^0 is the standard pressure [1013 mbar], ΔH_r^0 [J/mol] and ΔS_r^0 [J/K mol] are enthalpy and entropy of the reaction, respectively.

The works of Sögütoglu et al. [19,28] have shown that there are two main areas, where reaction proceeds differently: (1) inside MSZ – an area around equilibrium conditions (hatched area in Fig. 2) where any reaction is preceded by an induction period; (2) outside MSZ – zone past MSZ boundary (a plain grey area in Fig. 2), where the reaction is instantaneous. Due to significant differences in how the reaction proceeds in each area, they will be treated separately.

2.1. Dehydration inside the MSZ

Dehydration behaviour and the observed induction period in salt hydrates are commonly explained through the classical nucleation theory (CNT). The induction period τ [s] is defined as the time, which elapses between the achievement of supersaturation and the start of rapid desupersaturation due to the growth of the nucleus past its critical size [29]. The induction period is stochastic, and it can be expressed as [19]:

$$\tau \propto J^{-1}$$
 (2)

where J [s⁻¹] is the nucleation rate, which can be expressed as an Arrhenius-like reaction rate equation [19]:

$$J = \kappa \exp\left(-\frac{\Delta G^*}{k_B T}\right) \tag{3}$$

where κ [s⁻¹] is a kinetic parameter, ΔG^* [J] is the nucleation barrier, and k_B [1.38 \times 10⁻²³ J/K] is the Boltzmann constant.

Nucleation barrier ΔG^* is dependent on the size of the nucleus, interface between the nucleus and the mother phase, dictated by the interfacial tension γ [J/m²], the nucleus shape, which could be a 2D disk or a 3D (hemi)sphere, described by the shape factor ω , as well as the driving force $\Delta\mu$. In general terms, the nucleation barrier can be expressed as [29]:

$$\Delta G^* = \Delta G_{bulk} + \Delta G_{surface} = \frac{V}{v} (b - a) \Delta \mu + \gamma A \tag{4}$$

where V [m³] is the molecular volume of the cluster, ν [m³] is the volume of a single dehydrated unit, and A [m²] is the area of the cluster.

The driving force $\Delta\mu$ is dependent on temperature and vapour pressure according to the following relation:

$$\Delta \mu = \mu_{anh} - \mu_{hyd} = k_B T ln \left(\frac{p}{p_{eq}} \right) = k_B T ln(p^*)$$
 (5)

where p_{eq} [mbar] is the equilibrium vapour pressure at a given temperature, and the relationship between the applied vapour pressure p and the equilibrium pressure is called the supersaturation or driving

force, p*.

Depending on the shape of the nucleus, the nucleation barrier can be expressed as:

2D:
$$\Delta G^* = -\frac{h\pi v \gamma^2}{(b-a)k_B T ln(p^*)}$$
 (6)

$$3D: \Delta G^* = -\frac{\eta \pi v^2 \gamma^3}{\left[(b-a) k_B T \ln(p^*) \right]^2}$$
 (7)

where h [m] is the height of the nucleus and η is a shape factor where η =8/3 for hemisphere and η =16/3 for a sphere.

Complete derivations of those two relationships can be found in Supplementary information Appendix A. What both equations illustrate is that the nucleation barrier and thus the nucleation rate is dependent on driving force p^* [22]:

$$J = \kappa \exp\left(\frac{\lambda}{\left[\ln(p^*)\right]^n}\right) \tag{8}$$

where λ is a thermodynamic parameter that relates to ΔG^* , with n=1 or 2 reflecting the nucleus's shape for respectively 2D or 3D nucleation.

A close examination of Eq. (8) reveals that a critical level of supersaturation, p^*_{crit} , must be exceeded to have instantaneous nucleation [29]. At conditions where $p^* < p^*_{crit}$, nucleation will occur only after a certain induction period which can be related to the driving force as follows [19]:

$$\ln(\tau^{-1}) = \ln(\kappa) - \frac{\lambda}{\left[\ln(p^*)\right]^n} \tag{9}$$

2.2. Dehydration outside the MSZ

Outside of the MSZ, the dehydration process is usually described as a single step reaction with conversion, $\frac{d\alpha}{dt}$, being dependent on temperature and pressure in accordance with:

$$\frac{d\alpha}{dt} = f(\alpha)k(T)h(p) \tag{10}$$

Function f(a) describes conversion that could be conveyed according to one of the well-established models [30]. The temperature dependency, k(T), is often expressed in the form of the Arrhenius equation:

$$k(T) = A \exp\left(\frac{-E_a}{RT}\right) \tag{11}$$

where A is the preexponential factor, E_a is the apparent activation energy. The apparent activation energy is commonly extracted from reaction rate measurements at different temperatures using the van 't Hoff plot and the equation above. Nevertheless, very little attention is usually given to the reaction conditions, being vapour pressure and temperature, and their relation to equilibrium conditions. Moreover, the basic Arrhenius approach does not account for the entropic term of Gibbs energy.

In transition state theory (TST), the reaction rate r can be expressed

$$r = k_1 - k_2 \approx C \exp\left(\frac{-\Delta G_b^{\#}}{k_B T}\right) - C \exp\left(\frac{-\Delta G_a^{\#}}{k_B T}\right)$$
 (12)

where C is a constant and $\Delta G^\#$ is the change in Gibbs energy between the initial state b state and the transition state (TS) or final state a and TS. With further consideration of the forward and backward reactions (done in Supplementary information Appendix B), this relationship transforms into:

$$r = Cexp\left(-\frac{\Delta G_b^{\#}}{k_B T}\right) \left[1 - \left(\frac{p}{p_{eq}}\right)^{\nu}\right]$$
 (13)

where v = N(b - a)

 $\Delta G_b^{\#}$ is the free energy barrier for reactant b to transform to the transition state. Comparing Eqs. (11) and (13), we see similarities in the exponential term. However, TST underlines the importance of driving force (p/p_{eq}=p*) when determining the energy barrier, which is often neglected in the classical Arrhenius approach.

The influence of water vapour is often neglected, not only while extracting the Arrhenius parameters [31], but also when considering the pressure dependency term h(p) in Eq. (10), h(p). This oversight is quite frequent since many experiments are conducted under a constant flow of inert gas with the assumption that gasses produced during the reaction are removed from the reaction zone. Thus, their influence on the kinetics is less likely to be treated [5,32].

When accounted for, pressure dependency is most commonly defined as [4,5,28,33]:

$$h(\mathbf{p}) = 1 - \frac{p}{p_{ea}} \tag{14}$$

which is based on the assumption that the overall reaction rate of Reaction 2 is dependent on the difference between forward and reverse reaction and the vapour partial pressure of the gaseous product according to Vyazovkin [4]:

$$r = k_1 - k_2 p = k_1 \left(1 - \frac{p}{p_{eq}} \right) \tag{15}$$

Another form of pressure dependence previously encountered in the dehydrogenation of metal hydrides is [34–36]:

$$h(\mathbf{p}) = p_{eq} - p \tag{16}$$

This relationship can be related to Fick's first law of diffusion and suggests that the reaction rate is proportional to the difference between equilibrium pressure and partial vapour pressure.

Other forms of pressure dependence, or combinations thereof, have been used in the literature [4,26,34,37,38]. Many of those approaches are either purely empirical or modelling results. In our evaluation we chose to focus on the single-step reaction approach provided by CNT and TST as the first approximation of the problem.

3. Materials and methods

 $K_2 CO_3$ used in this study was purchased from Sigma-Aldrich. The asreceived powder was ground in pestle and mortar and sieved between 50 and 164 μm particle fraction. Approximately 5 mg of this powder was then loaded into a 40 μL Mettler-Toledo standard aluminium pan without a lid, which was then loaded into a thermogravimetric analyser (TGA).

Reaction kinetics were studied in TGA 851e by Mettler-Toledo, which is coupled with an external, in-house built humidifier. The devices operate with a nitrogen atmosphere at a fixed flow rate of 300 mL/min. The temperature of TGA was calibrated using an SDTA signal of melting points of naphthalene, indium, and zinc. The humidifier was calibrated by establishing deliquescence point of LiCl·H₂O, $K_2CO_3 \cdot 1.5H_2O$, $MgCl_2 \cdot 6H_2O$ and $Mg(NO_3)_2 \cdot 6H_2O$ salt hydrates at $25^{\circ}C$ [39].

Before investigating dehydration kinetics, the sample was subjected to 20 (de)hydration cycles to minimise the effects of initial powder morphology [6,40]. During the cycling, hydration was conducted at 30 $^{\circ}\text{C}$ and 12 mbar water vapour pressure, while dehydration was conducted at 125 $^{\circ}\text{C}$ and 0 mbar.

The dehydration measurements are into (1) isobaric-isothermal measurements within MSZ and (2) isobaric-isothermal measurements outside MSZ. The conditions at which all measurements were conducted are indicated in Fig. 3.

In total, 14 isobaric-isothermal measurements were conducted inside

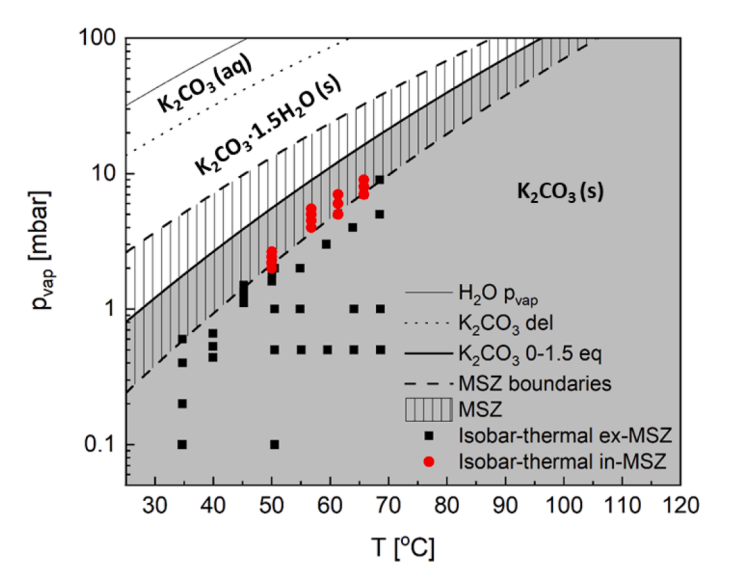


Fig. 3. K_2CO_3 pressure-Temperature phase diagram adapted from Sögütoglu et al. [19]. p_{vap} is vapour pressure, and T is sample temperature. The equilibrium line between anhydrous and hydrated K_2CO_3 is drawn as a thick black line, and the dashed area indicates the metastable zone (MSZ). Red points indicate isobaric-isothermal kinetic measurements inside MZS, and black points indicate isobaric-isothermal kinetic measurements outside MZS.

MSZ (Red dots in Fig. 3) that were used to evaluate reaction kinetics and 28 outside MSZ (Black squares in Fig. 3). Six of those points are at the edge of MSZ to better understand reaction development over a wider range of vapour pressures at a fixed vapour pressure. All those measurements follow the same protocol, illustrated in Fig. 4. First, the sample is fully dehydrated *in-situ* for 60 min at 130 °C and 0mbar. Subsequently, it is fully hydrated for 60 min at 40 °C and 19 mbar. Then, the temperature is adjusted to desired conditions, and the sample is equilibrated for 30 min at the selected temperature and 19 mbar vapour pressure. Only then humidity with desired water content is introduced to the system. This point marks t=0 for further analysis purposes. To pinpoint the exact conditions at which the measurement is conducted, measured sample temperature and applied vapour pressure are used for analysis.

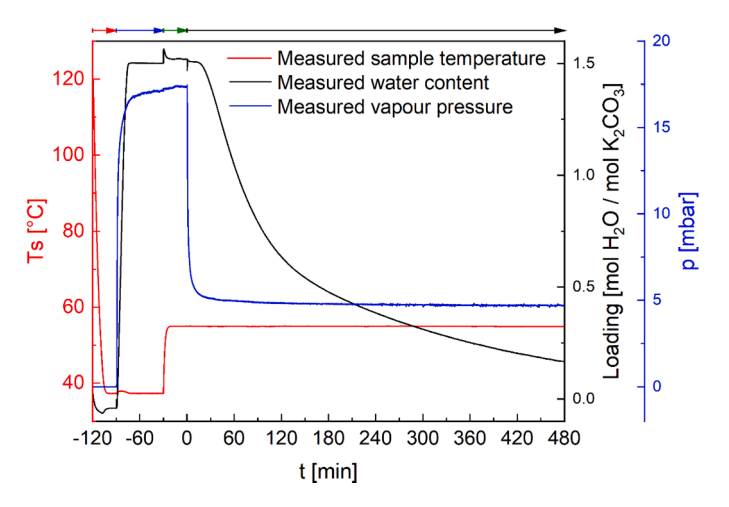


Fig. 4. An example of measurement at isobaric-isothermal conditions at $57\,^{\circ}\mathrm{C}$ and $5\,$ mbar. The black plot shows calculated changes in loading based on the measured mass changes, the red plot is the measured sample temperature, and the blue plot is the measured vapour pressure at the outlet of the TGA. The red arrow indicates the dehydration period, the blue arrow indicates the hydration period, a green arrow indicates the settling period, and the black arrow indicates the measurement period.

Ultimately, K_2CO_3 powder used in the TGA is investigated with scanning electron microscopy (SEM) to understand the morphology changes with dehydration and cycling. For this purpose, two powder samples were selected: a pristine K_2CO_3 powder that was ground and sieved identically as the samples for TGA analysis and a K_2CO_3 powder that was ground, sieved and subjected to 20 (de)hydration cycles in TGA, which is analogous to the starting material for dehydration experiments. Before SEM imaging, powder samples were completely dehydrated in an oven at $130\,^{\circ}$ C. Samples were then fixed to a stub with carbon tape and immediately placed in the SEM to prevent any hydration. The images were taken with JEOL Fei Quanta 600. For the measurement high vacuum, 5 kV accelerating current and 3.0 spot size were used.

The imaging study was supplemented with N₂ adsorption surface area analysis conducted in Micrometerics' Gemini. For this analysis approximately 5 g of powder was cycled. Hydration was conducted in a desicator with saturated MgCl₂·6H₂O solution (approximately 8 mbar at 21 °C [39]) and subsequently dehydrated in an oven at 130 °C. Prior to the analysis, sample was dehydrated and degassed overnight at 130 °C under constant N₂ flow.

4. Results

4.1. The structure of uncycled and cycled K₂CO₃

Since the morphology of K_2CO_3 particles changes with cycling, which can impact kinetics [3], we have investigated K_2CO_3 powder used in TGA measurements with SEM to get an impression of the morphology applicable to our study. In Fig. 5 images obtained at 1000x magnification (top) and 5000x magnification (bottom) of uncycled (left) and cycled (right) are presented. The most important observation is the severe change in powder morphology with cycling. The uncycled powder has a fairly closed structure with very little porosity. After cycling, the surface area increases drastically, and more voids are built into the material. At this point, it is hard to observe individual particles as many of them have merged into larger, interconnected agglomerates. The surface becomes much rougher as pores and channels leading into the agglomerate can be seen in many areas. Similar observations have been made in earlier studies investigating morphological changes of K_2CO_3 with cycling [7,40].

To better understand the changes in morphology in relation to the available surface area we have conducted N_2 adsorption measurements. Results of that analysis are summarised in Table 1. They confirm that the the surafe area increases with cycling, as seen in the SEM images in Fig. 5. In both cases the pore volume is extremaly low, which can be deduced from the SEM images as well. The voids that are seen to develop with cycling are in micrometre scale, and are likely the effect of cracking of large particles, observed in earlier studies \cite{T} and coalescence of smaller ones.

Through this joint analysis we learn that the morphology of the pristine powder undergoes significant changes with repetitive (de)hydrations. It becomes more open and the surface area increases making the solid more accessible to the gasses in its surroundings. At the same time a greater surface area should make removal of water vapour generated during dehydration easier and prevent diffusional issues that are often encountered in larger particles [18].

4.2. Dehydration kinetics within MSZ

Within the MSZ, we evaluate dehydration at a relatively high vapour pressure compared to equilibrium conditions. In this zone, the overall process is characterised by two attributes: (1) an induction period, τ , at the beginning of each measurement and (2) a subsequent reaction rate, as illustrated in Fig. 6. The measurements within MSZ are conducted at four different temperatures (50, 57, 61 and 66 °C, red dots in Fig. 3). Before a measurement starts, the sample is fully hydrated *in situ* at 40 °C

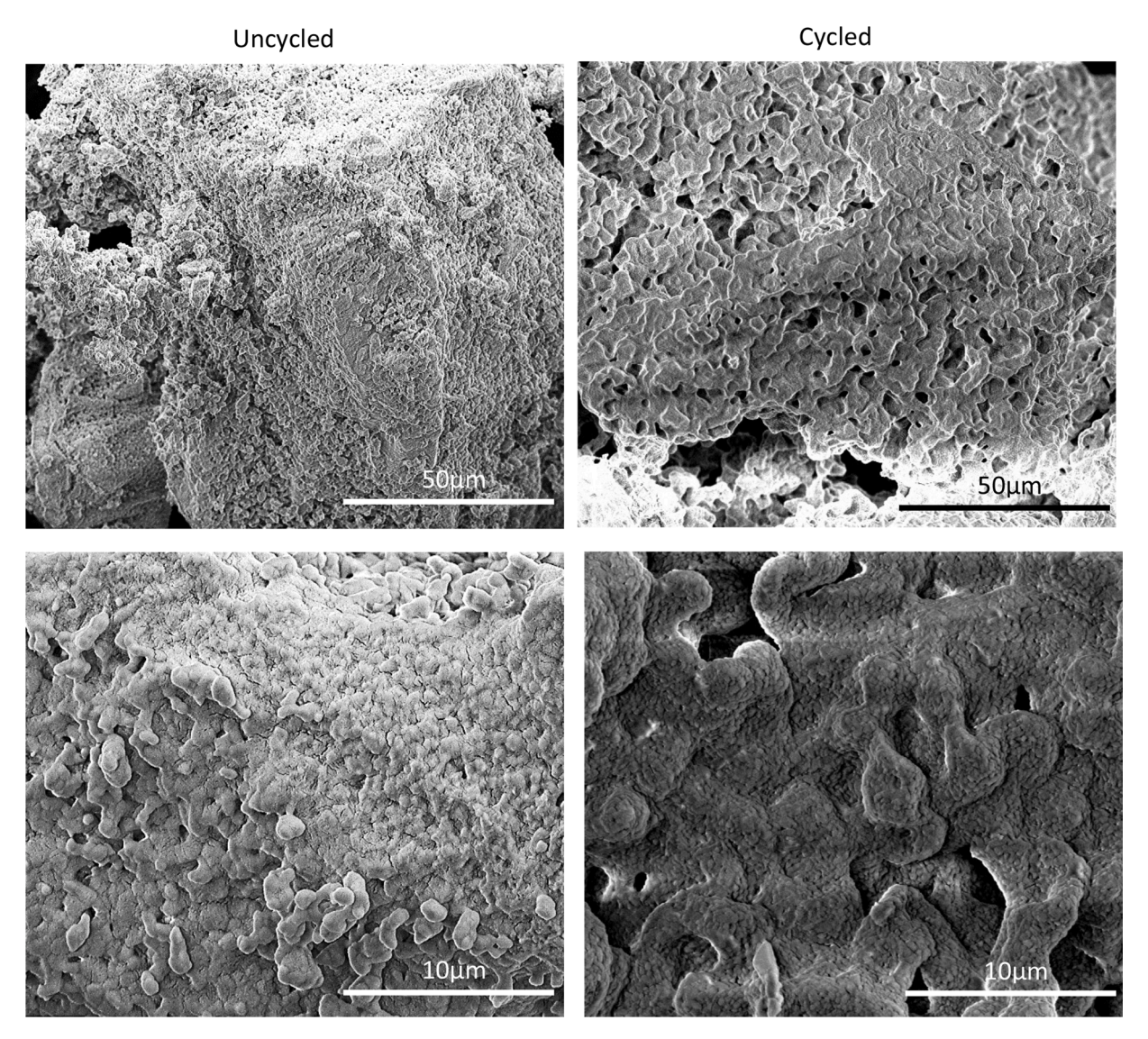


Fig. 5. SEM images of uncycled powder (left) and cycled powder (right) of anhydrous K₂CO₃ at 1000x (top) and 5000x (bottom) magnification.

 $\label{eq:table 1} \textbf{Summary of N_2 soprtion analysis performed on uncycled and cycled samples}.$

Uncycled 0.25 0.31	Sample	BET surface area [m ² /g]	BJH pore volume [mm ³ /g]
Cycled 0.77 0.52	Uncycled Cycled		

and 19 mbar. Subsequently, the desired temperature is equilibrated for 30 min, after which the vapour pressure is lowered, and measurement begins.

From the measured data, we have determined the length of the induction period τ as the point of intersection between baseline at a stable loading of 1.5 mol H₂O/mol K₂CO₃ and a tangent at an inflexion point in the reaction rate curve (Red tangent lines on the dashed plot in Fig. 6).

The derived induction periods are summarised in Fig. 7. This representation shows an exponential increase in the duration of the induction period with increasing pressure at a fixed temperature. A similar correlation has been observed previously for K_2CO_3 hydration [19] and many other salt hydrates [5,41,42]. The presence of an induction period is linked to CNT [22]. It is often explained as the time required for a nucleus to form and to start growing, which manifests itself as mass loss in our measurements. The corresponding maximum reaction rates, shown in Fig. 7b, show a nearly linear decrease with increasing pressure

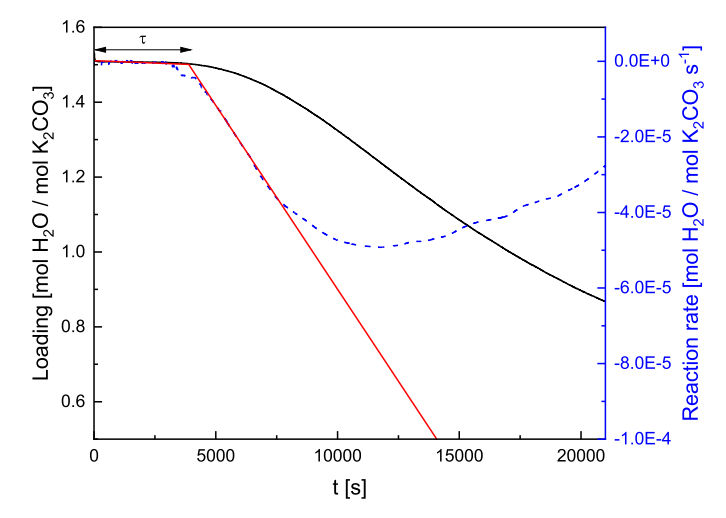


Fig. 6. An example of induction time measurements at 57 $^{\circ}$ C and 4.5 mbar. The solid curve shows a change in loading, the dashed curve show change in dehydration rate vs time. The red tangents indicate the principle used to determine the length of an induction period.

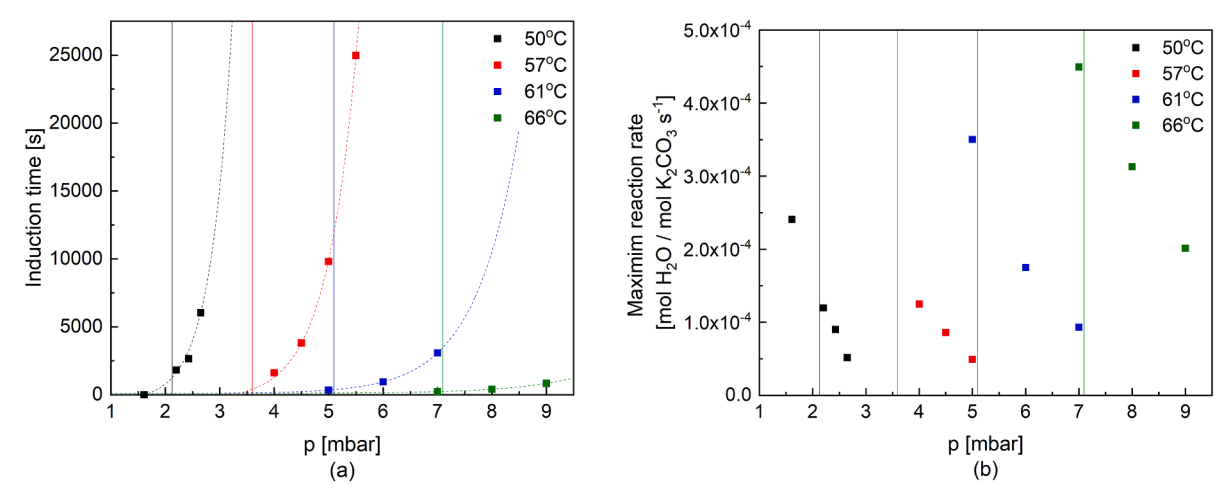


Fig. 7. Measured (a) induction period and (b) maximum reaction rates at isobaric-isothermal conditions at four different temperatures (50 °C – black, 57 °C – red, 61 °C – blue, 66 °C – green). The solid lines indicate the edge of MSZ for the respective temperatures. The dashed lines connecting the points are just a guide for the eye. Note that most of the measurement time at 57 °C and 5.5 mbar was consumed by the induction period; therefore, the reaction rate could not be measured.

at a fixed temperature. Similar observations have been made for dehydration and decomposition processes in the presence of water vapour of other inorganic compounds [37,43]. It suggests that the reaction rate scales with induction period and that the nucleation of anhydrous K_2CO_3 is a limiting step [13]. Since dehydration of K_2CO_3 is a reversible process it could be argued that equilibrium presented in Rx. 1 is shifted towards reverse reaction which will impact both nucleation and reaction rates [4].

The applicability of CNT for this case can be tested through the relationship presented in Eq. (9). Here a linear correlation between inverse induction time and supersaturation is expected. In Fig. 8, we see that such a relationship does indeed exist for each investigated temperature in both models. This means that the explanation for the dehydration process provided by CNT is appropriate within the MSZ. From this relation, we can extract surface tensions, γ , which vary between 9 mJ/m² for 3D nucleus to 22 mJ/m² for 2D nucleus, as shown in Table 2, which is comparable with previously published values [19].

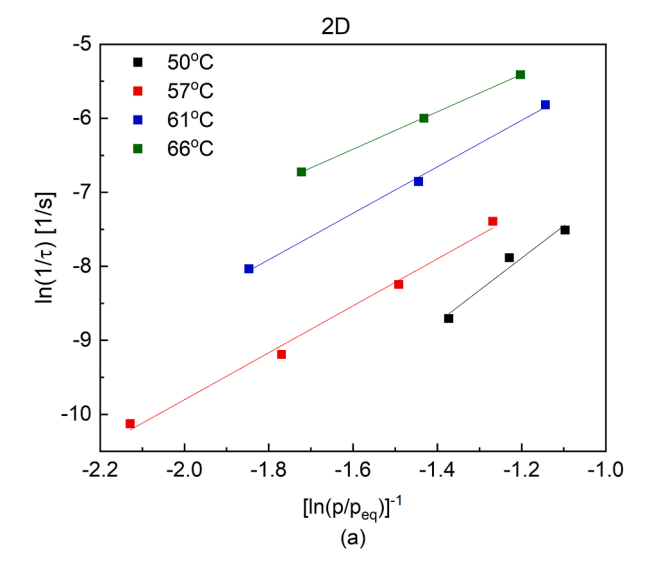
Based on literature, a decrease in surface tenstion is expected with increasing temperature [19]. However, given the error values the calculated surface tenraions for each geometry are relatively constant.

A further evaluation of induction periods and their relationship with

Table 2 Surface tensions γ for 2D and 3D nucleus based on Eqs. (6) and (7) and Fig. 8 together with R^2 values for the corresponding linear fits at given sample temperature T.

T [°C]	2D [mJ/ m ²]	R ²	3D hemisphere [mJ/m²]	3D sphere [mJ/m²]	R ²
50	$\begin{array}{c} 21.7 \pm \\ 9.5 \end{array}$	0.96497	11.2 ± 5.5	8.9 ± 4.4	0.97379
57	$18.9 \pm \\4.7$	0.99218	11.9 ± 5.9	9.5 ± 4.7	0.99678
61	$\begin{array}{c} 19.0 \ \pm \\ 4.1 \end{array}$	0.99790	11.3 ± 4.4	9.0 ± 3.5	0.98587
66	$17.3 \pm \\1.5$	0.99970	14.7 ± 7.9	11.7 ± 6.3	0.97582

the dehydration rate is done in Fig. 9, which gives us an insight into the growth process which occurs right after nucleation. We observe a nearly linear relationship between the maximum dehydration rate and the inverse induction time. At a fixed temperature, the reaction rate increases with decreasing induction time, which shows that within MSZ, nucleation of the anhydrous phase limits the reaction rate [19].



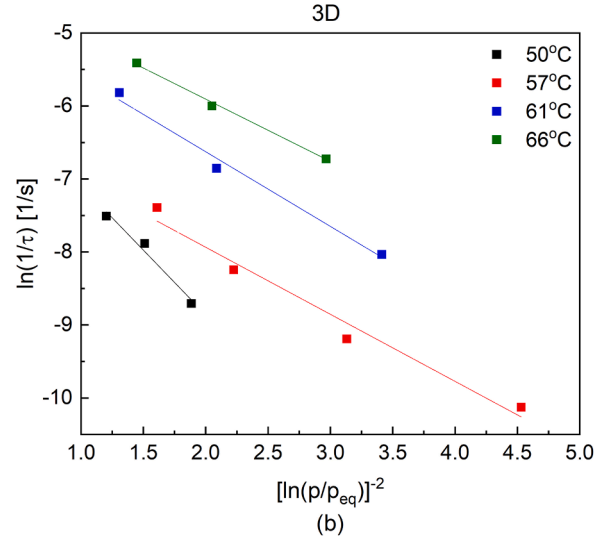


Fig. 8. Measured inverse induction time vs $(\ln(p/p_{eq}))^n$ at different temperatures (50 °C – black, 57 °C – red, 61 °C – blue, 66 °C – green) according to Eq. (9), together with linear fits assuming (a) 2D nucleation and (b) 3D nucleation.

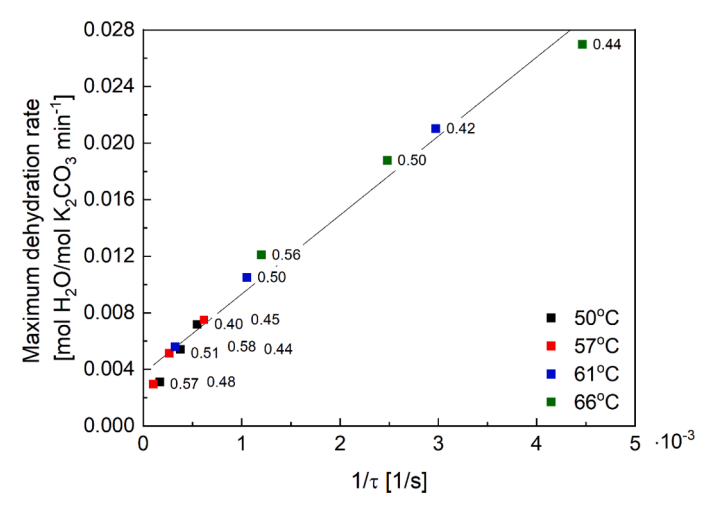


Fig. 9. Maximum dehydration rates inside MSZ at four different temperatures (50 $^{\circ}$ C – black, 57 $^{\circ}$ C – red, 61 $^{\circ}$ C – blue, 66 $^{\circ}$ C – green) as a function of the inverse induction time. p/p_{eq} for the measurement is indicated as a label next to the data point, while the thin black line is a linear fit of the data with R^2 =0.98057.

4.3. Dehydration pathways

In the previous section, we have considered only the maximum dehydration rate in our evaluation in Fig. 9, but this does not provide the entire picture. Considering the change in reaction rate as a function of loading, as illustrated on the top of Fig. 10, we can see a trend developing. At high driving forces, meaning far from MSZ, the reaction rate is relatively constant throughout the entire process, indicating a predominantly growth limited dehydration process. Deviations from constant dehydration rate observed at the start of dehydration, even at very low p/p_{eq} are partly caused by the measurement error as it requires several minutes for the atmosphere withing the TGA oven to equilibrate. On the other hand, diffusion issues cannot be fully excluded.

As we move closer to the MSZ, the reaction rate drops off at much higher loading (lower conversion), ranging from 1 to 1.2 mol $\rm H_2O$ / mol $\rm K_2CO_3$. If we consult the corresponding loading vs time curves on the bottom of Fig. 10, we observe increasing tailing in the mass loss. Those differences in dehydration pathways indicate that different processes limit the process at different driving force ranges.

4.4. Dehydration kinetics

Based on the evaluation of reaction pathways inside and outside the MSZ, we have determined that dehydration of K_2CO_3 powder is

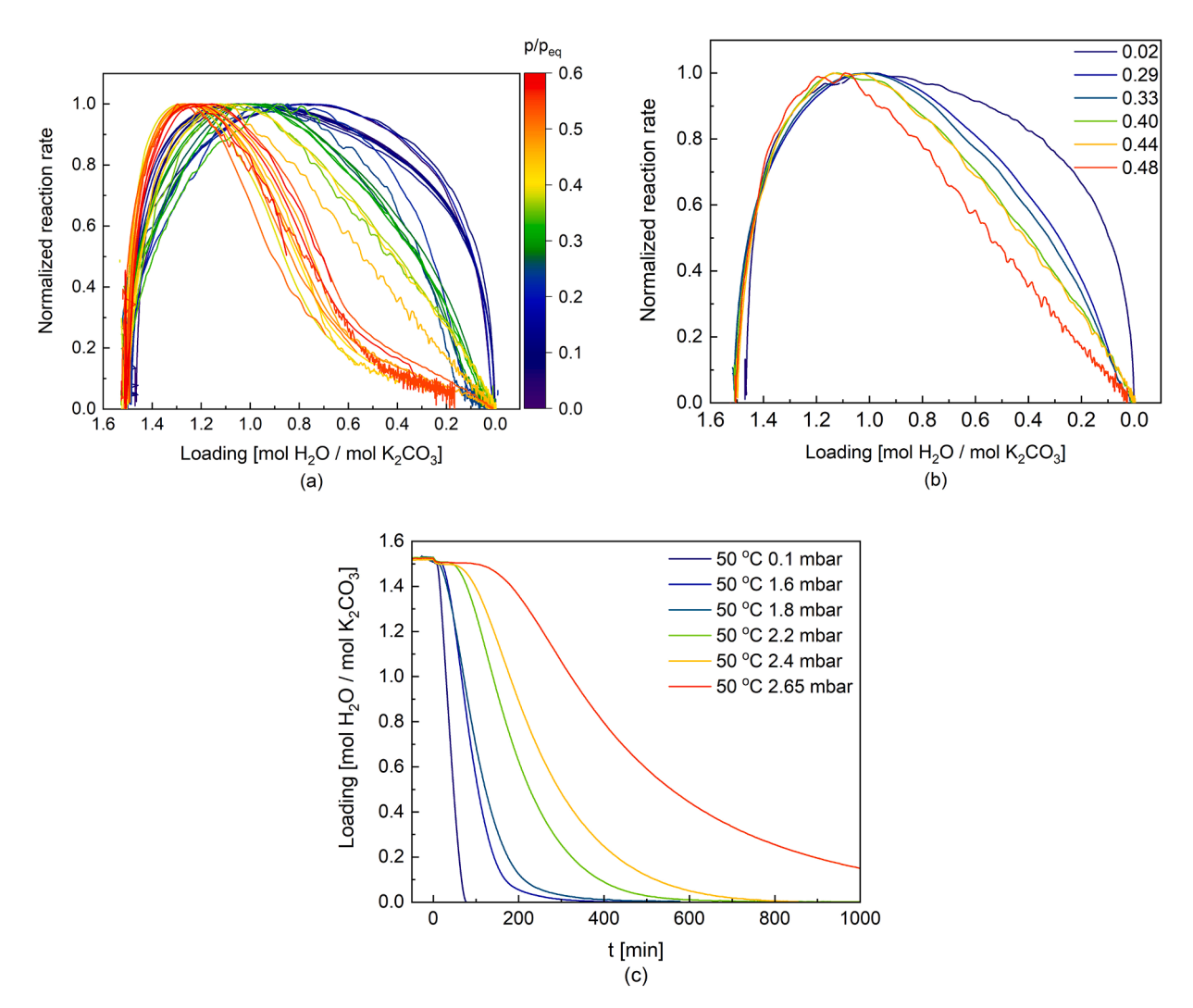


Fig. 10. (a) Reaction rate plots normalised to the maximum rate as a function of loading colour coded according to $p/p_{\rm eq}$ indicated in the legend. Example of analysis on data collected at 50 °C and different $p_{\rm vap}$ (b) normalised reaction rate as a function of loading with $p/p_{\rm eq}$ indicated in the legend (c) corresponding loading as a function of time with vapour pressures shown in the legend.

predominantly reaction limited. It means that the activation energy E_a can be extracted through TST and Arrhenius analysis. In Fig. 11, we plotted the maximum dehydration rates and colour-coded them according to p/p_{eq} , which is also indicated in the label. Lyakhov et al. [31] have postulated that the assumption of a linear relationship between reaction rate and 1000/T in the Arrhenius equation is valid only in a narrow p-T range or at comparable p/p_{eq} values (p/p_{eq} \pm 0.02). With this in mind, we have selected several narrow p/peq zones to calculate the apparent activation energy. The resulting linear fits show that the apparent activation energy decreases with increasing driving force, or decreasing $p/p_{eq}.$ It levels off at 78.5 kJ/mol when $p/p_{eq} < 0.1, \ also$ presented in the insert in Fig. 11 as p_{eq}/p . Those observations agree with remarks made by Lyakhov et al. [31] and observations made by Galway [44], showing that there is no universal activation energy for a dehydration process but that it is strongly dependent on the reaction conditions. Furthermore, the values obtained outside MSZ are comparable with the activation energies reported in earlier studies which were in the range of 78.3-92 kJ/mol [8,18,14], which is, as expected, somewhat higher than the reaction enthalpy 65.8 kJ/mol [6].

In Fig. 12, the apparent activation energy is evaluated as a function of loading at several selected p/peq that correspond to the fits presented in Fig. 11. At very low p/peq (navy plots), the apparent activation energy is constant throughout the entire process and equal to approximately 77 kJ/mol, similar to what was established earlier. As the driving force decreases and p/peq increases, a dependence of $E_{\rm a}$ on loading emerges. This is particulatly noticeable for measurements conducted inside MSZ (orange plots) where the the $E_{\rm a}$ increases with increasing conversion.

If we then consider the reaction rate as a function of driving force, as we did in Fig. 13a, we see a linear relationship between the maximum reaction rate and p/p_{eq} for each temperature. However, as the p/p_{eq} decreases, the effect of vapour pressure on the dehydration rate decreases, as shown in Fig. 13b. In addition, we notice that the maximum reaction rate stabilises for p_{eq}/p >10 (p/p_{eq} <0.1, navy plots), which corresponds with the findings for stabilisation of E_a for p_{eq}/p >8 in Fig. 11.

5. Discussion

In this study, we have conducted a series of isobaric-isothermal measurements within and outside of MSZ. Each measurement within MSZ begins with an induction period, meaning that although thermodynamically, the conditions are suitable for dehydration to take place, it

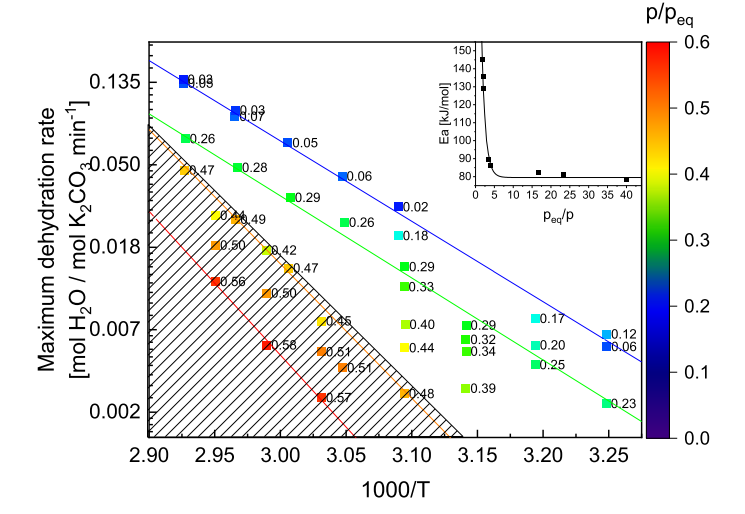


Fig. 11. Arrhenius type plot based on maximum reaction rate at isobaric and isothermal conditions. Hatched area indicates MSZ, data points are colour coded according to $p/p_{\rm eq}$, and colour lines show linear fit used to calculate apparent activation energies shown in the insert as a function of $p_{\rm eq}/p$.

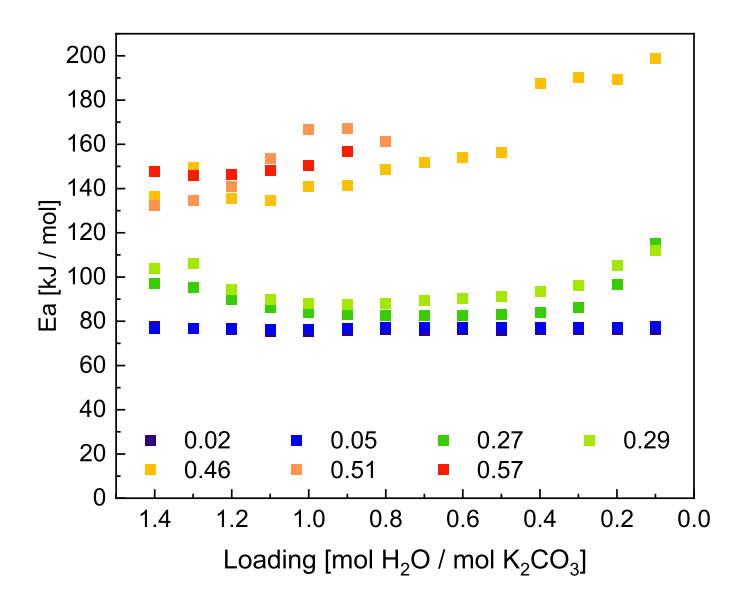


Fig. 12. Apparent activation energy E_a as a function of loading for selected regimes of $p/p_{\rm eq}$ listed in the legend.

does not occur immediately. This presence of the induction period implies several things. Firstly, close to equilibrium conditions, the reaction is limited by nucleation, as shown in Fig. 9. Secondly, the dehydration behaviour in this region can be explained with the aid of CNT. Thirdly, the apparent activation energies within MSZ, obtained in Fig. 11, are a compound of the activation energy for the reaction and the added threshold in from of nucleation barrier, which increases with increasing proximity to the equilibrium conditions, resulting in elevated E_a values.

Outside of MSZ, dehydration is no longer limited by the nucleation of the anhydrous phase but by the further growth of the anhydrous phase itself at the expense of the hydrate. This is, on the one hand, inferred from Fig. 10, where the reaction rate is nearly constant throughout the entire process, while on the other hand, it becomes insensitive to the driving force when $p/p_{\rm eq}<0.1,$ as shown in Fig. 11.

Finally, if we evaluate dehydration pathways at different driving forces, we see that the reaction might not be a single-step process as it is commonly believed. In Fig. 10, we see that as the driving force decreases, a clear maximum in the dehydration rate at approximately 33% of conversion appears, which is followed by a gradual decrease in the reaction rate. There are two possible reasons for that kind of behaviour: diffusion limitation or reaction limitation. Typically, this behaviour is described with the aid of a shrinking core model, which could give rise to diffusion limitation during dehydration [8,18]. However, if the dehydration far outside the MSZ is principally reaction limited, the same should apply to a broader range of driving forces. However, as we move into MSZ, the driving force for dehydration becomes insufficient for the entire process to proceed at a constant rate suggesting a multistep process taking place. Further corroboration for that theory can be found in Fig. 12, which shows an abrupt change in apparent Ea around 0.5 mol H₂O / mol K₂CO₃ when measurement is conducted inside MSZ.

There are indications in early literature that dehydration of $K_2CO_3 \bullet 1.5H_2O$ is a multistep process. In their study, Deshpande et al. [14] showed that K_2CO_3 dehydrates in 2 steps of 0.5 and 1 mol of H_2O , each with its own activation energy. However, they did point out that the calculated activation energy depends on the measurement conditions and the assumptions made during the calculations, a factor that has not been accounted for by Stanish et al. [18] or Gaeini et al. [8]. Furthermore, they have postulated that dehydration of K_2CO_3 crystals is a nucleation and growth process, which agrees well with our own observations. Interestingly, the thermodynamic equilibrium line for K_2CO_3 0 - 0.5 H_2O transition, based on values obtained by Thomsen [16], coincides well with the more recently established MSZ boundary for

60

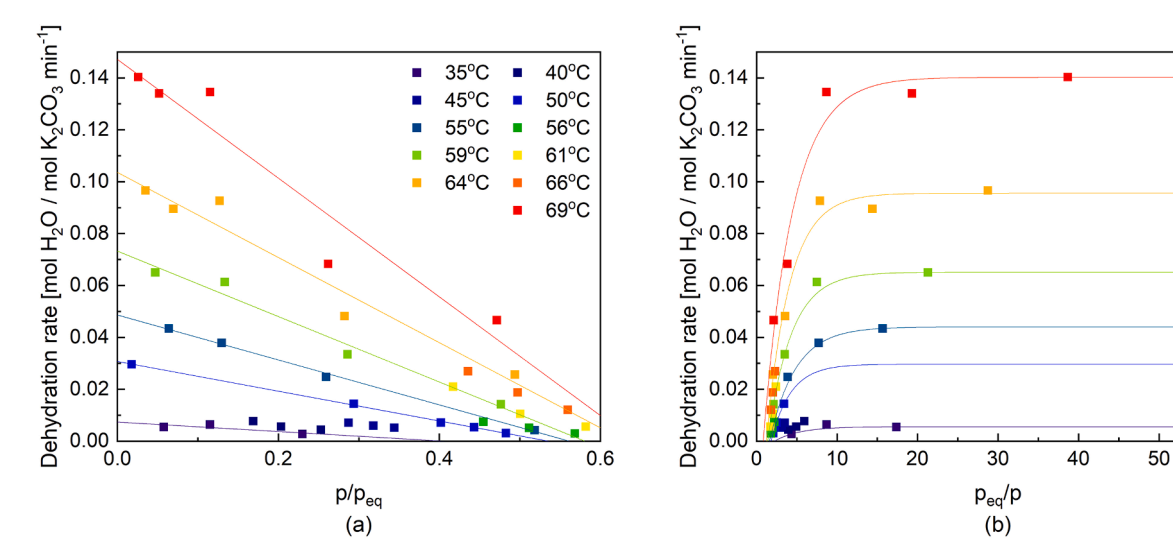


Fig. 13. Maximum dehydration rate as a function of (a) p/p_{eq} and (b) p_{eq}/p at different temperatures.

dehydration [19]. Therefore, although there is no conclusive evidence for the existence of lower hydrates of K_2CO_3 , we cannot exclude a metastable hydration state.

To evaluate the possibility of multistep dehydration, we take a closer look at the crystal structure of $K_2CO_3 \bullet 1.5H_2O$, shown in Fig. 14. At first glance, all water molecules seem to be arranged in a single plane. However, a closer investigation shows that we potentially have two different environments within that plane. The black circle in Fig. 14 marks the first environment that includes $^1/_3$ of those molecules, which form a single file through the structure. The green circles mark the remaining $^2/_3$ of water molecules, which are arranged as a double file of two channels mirroring each other. If we compare that with the consistent dehydration maximum at approximately 1mol H_2O / mol K_2CO_3 in Fig. 10, we see that $^1/_3$ of water molecules is released easier or faster than the remaining $^2/_3$. Such a process does not have to involve a new crystal phase in K_2CO_3 . Nevertheless, a metastable phase of $K_2CO_3 \bullet H_2O$ or $K_2CO_3 \bullet 0.5H_2O$ that requires a higher energy input could

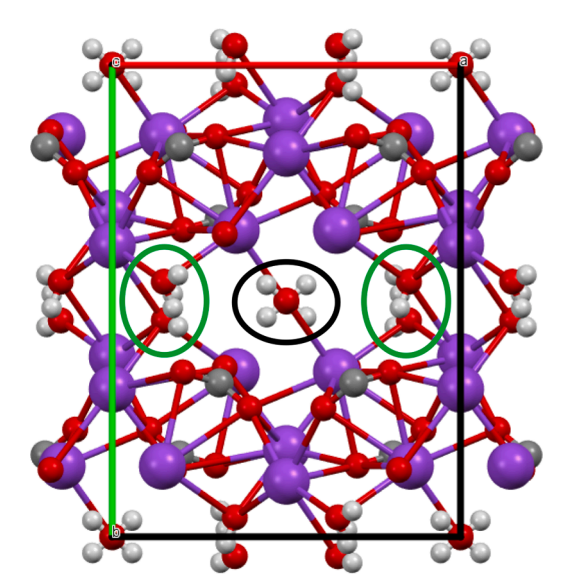


Fig. 14. Crystal structure of K_2CO_3 •1.5 H_2O , showed along c-axis, based on ICSD-280789 and generated in Mercury software. The unit cell axes are a-red and b-green. The atom colours are: potassium-purple, carbon-grey, oxygen-red and hydrogen-white. The $^1/_3$ of water molecules forming a channel through the structure are marked with a black circle. The remaining $^2/_3$ or water molecules are marked with a green circle.

be formed.

From a practical point of view, knowing the limitations in the different vapour pressure and temperature regimes allows for more targeted problem-solving. Based on our study, the main limitation to dehydration, provided particle size is small enough to avoid diffusional issues, arises from the phase transformation on the crystal level. It implies that to resolve this issue, an approach that impacts K_2CO_3 on a molecular level has to be developed.

6. Conclusion

In this work, we have evaluated the effect of water vapour pressure on the dehydration behaviour of K2CO3·1.5H2O. Through a series of isobaric-isothermal measurements at fixed points close to the equilibrium conditions, we have established that within MSZ, the reaction is limited by the nucleation rate, and the process can be explained through CNT. The nucleation barrier disappears when the MSZ boundary is crossed, and the reaction begins instantaneously. In this region, the rate is limited by the reaction speed itself. Nevertheless, a sufficiently high driving force must be provided for the reaction to proceed at a constant rate. It has been estimated that for $\ensuremath{p/p_{eq}}\xspace<0.1,$ both reaction rate and apparent activation energy are relatively constant and do not change with decreasing p/peq. If the driving force is not sufficiently high, the dehydration rate seemingly proceeds in two or three steps, and it is limited by the removal of the last 0.5 mol of H₂O. To verify this theory, a thorough investigation with atomistic simulations should be conducted. Based on our experimental work, we can conclude that dehydration of K₂CO₃ is a multistep process, whose activation energy is strongly dependent on reaction conditions and where water vapour plays a crucial role.

CRediT authorship contribution statement

Natalia Mazur: Conceptualization, Methodology, Validation, Investigation, Visualization, Writing – original draft, Writing – review & editing. Henk Huinink: Conceptualization, Writing – review & editing, Supervision, Funding acquisition. Bart Borm: Methodology, Validation, Investigation. Stefano Sansota: Conceptualization, Writing – review & editing. Hartmut Fischer: Conceptualization, Writing – review & editing, Supervision. Olaf Adan: Conceptualization, Writing – review & editing, Funding acquisition.

Declaration of Competing Interest

The authors declare that they have no known competing financial interests or personal relationships that could have appeared to influence the work reported in this paper.

Acknowledgments

This publication is part of the project Mat4Heat with project number 739.017.014 of the research programme Mat4Sus which is financed by the Netherlands Research Council (NWO).

The authors thank Hans Dalderop for his technical support.

Supplementary materials

Supplementary material associated with this article can be found, in the online version, at doi:10.1016/j.tca.2022.179286.

References

- B. Topley, M.L. Smith, Function of water vapour in the dissociation of a salt hydrate, Nature 128 (1931) 302, https://doi.org/10.1038/128302a0.
- [2] J. Colvin, J. Hume, The dehydration of salt hydrates, Trans. Faraday Soc. 34 (1938) 969–976.
- [3] T.B. Benjamin, M.J. Lighthill, Nucleation phenomena arising during the dehydration of solid hydrates, Proc. R. Soc. London. Ser. A. Math. Phys. Sci. 224 (1954) 460–471, https://doi.org/10.1098/rspa.1954.0173.
- [4] S. Vyazovkin, Kinetic effects of pressure on decomposition of solids, 10.1080/ 0144235X.2019.1691319, 39 (2019) 35–66, 10.1080/0144235X.2019.1691319.
- [5] G.D. Preturlan, L. Vieille, S. Quiligotti, L. Favergeon, J.G.D. Preturlan, L. Vieille, S. Quiligotti, L. Favergeon, Kinetics and mechanism of the dehydration of calcium sulfate dihydrate: a comprehensive approach for studying the dehydration of ionic hydrates under controlled temperature and water vapor pressure, 124 (2020) 26352–26367. https://pubs.acs.org/doi/full/10.1021/acs.jpcc.0c09041 (accessed June 4, 2021).
- [6] L.C. Sögütoglu, P.A.J. Donkers, H.R. Fischer, H.P. Huinink, O.C.G. Adan, In-depth investigation of thermochemical performance in a heat battery: cyclic analysis of K₂CO₃, MgCl₂ and Na₂S, Appl. Energy 215 (2018) 159–173, https://doi.org/ 10.1016/j.apenergy.2018.01.083.
- [7] M.A.J.M. Beving, A.J.H. Frijns, C.C.M. Rindt, D.M.J. Smeulders, Effect of cycle-induced crack formation on the hydration behaviour of K₂CO₃ particles: experiments and modelling, Thermochim. Acta 692 (2020), 178752, https://doi.org/10.1016/j.tca.2020.178752.
- [8] M. Gaeini, S.A. Shaik, C.C.M. Rindt, Characterization of potassium carbonate salt hydrate for thermochemical energy storage in buildings, Energy Build. 196 (2019) 178–193, https://doi.org/10.1016/j.enbuild.2019.05.029.
- [9] A.I. Shkatulov, J. Houben, H. Fischer, H.P. Huinink, Stabilization of K₂CO₃ in vermiculite for thermochemical energy storage, Renew. Energy 150 (2020) 990–1000, https://doi.org/10.1016/j.renene.2019.11.119.
- [10] K. Kant, A. Shukla, D.M.J. Smeulders, C.C.M. Rindt, Performance analysis of a K₂CO₃-based thermochemical energy storage system using a honeycomb structured heat exchanger, J. Energy Storage 38 (2021), 102563, https://doi.org/10.1016/J. EST 2021.102562
- [11] L. Scapino, H.A. Zondag, J. Van Bael, J. Diriken, C.C.M. Rindt, Sorption heat storage for long-term low-temperature applications: a review on the advancements at material and prototype scale, Appl. Energy 190 (2017) 920–948, https://doi. org/10.1016/j.apenergy.2016.12.148.
- [12] R.J. Clark, A. Mehrabadi, M. Farid, State of the art on salt hydrate thermochemical energy storage systems for use in building applications, J. Energy Storage 27 (2020), 101145, https://doi.org/10.1016/j.est.2019.101145.
- [13] A.K. Galwey, Structure and order in thermal dehydrations of crystalline solids, Thermochim. Acta 355 (2000) 181–238, https://doi.org/10.1016/S0040-6031(00) 00448 2
- [14] D.A. Deshpande, K.R. Ghormare, N.D. Deshpande, A.V Tankhiwale, Dehydration of crystalline K₂CO₃.1.5 H₂O, 66 (1983) 255–265.
- [15] J.J. Pohl, Chemische notizen, J. Prakt. Chem. 82 (1861) 148–170, https://doi.org/ 10.1002/PRAC.18610820120.
- [16] J. Thomsen, Thermochemische untersuchungen. XXVIII. Ueber die constitution der wasserhaltigen salze, J. Prakt. Chem. 18 (1878) 1–63, https://doi.org/10.1002/ PRAC.18780180101.
- [17] A.E. Hill, Hydrated potassium sesquicarbonate, K₂CO₃·2KHCO₃·3/2H₂O, J. Am. Chem. Soc. 52 (1930) 3817–3825, https://doi.org/10.1021/ja01373a008.
- [18] M.A. Stanish, D.D. Perlmutter, Kinetics and transport effects in the dehydration of crystalline potassium carbonate hydrate, AIChE J. 29 (1983) 806–812, https://doi. org/10.1002/aic.690290515.

- [19] L.C. Sögütoglu, M. Steiger, J. Houben, D. Biemans, H.R. Fischer, P. Donkers, H. Huinink, O.C.G. Adan, Understanding the hydration process of salts: the impact of a nucleation barrier, Cryst. Growth Des. 19 (2019) 2279–2288, https://doi.org/ 10.1021/acs.cgd.8b01908.
- [20] M. Richter, E.M. Habermann, E. Siebecke, M. Linder, A systematic screening of salt hydrates as materials for a thermochemical heat transformer, Thermochim. Acta 659 (2018) 136–150, https://doi.org/10.1016/j.tca.2017.06.011.
- [21] A.K. Galwey, M.E. Brown. Thermal Decomposition of Ionic Solids: Chemical Properties and Reactivities of Ionic Crystalline Phases, Elsevier, 1999.
- [22] W.J. Dunning, Nucleation and growth processes in the dehydration of salt hydrate crystals, Kinetics of Reactions in Ionic Systems (1969) 132–155, https://doi.org/ 10.1007/978-1-4899-6461-8 7.
- [23] L. Okhrimenko, L. Favergeon, K. Johannes, F. Kuznik, M. Pijolat, Thermodynamic study of MgSO₄ – H₂O system dehydration at low pressure in view of heat storage, Thermochim. Acta 656 (2017) 135–143, https://doi.org/10.1016/J. TCA 2017 08 015
- [24] J. Xu, T. Li, T. Yan, J. Chao, R. Wang, Dehydration kinetics and thermodynamics of magnesium chloride hexahydrate for thermal energy storage, Sol. Energy Mater. Sol. Cells 219 (2021) 110819, https://doi.org/10.1016/j.solmat.2020.110819.
- [25] T.S. Yan, T.X. Li, J.X. Xu, J.W. Chao, Understanding the transition process of phase change and dehydration reaction of salt hydrate for thermal energy storage, Appl. Therm. Eng. 166 (2020), https://doi.org/10.1016/j.applthermaleng.2019.114655.
- [26] S. Kodani, S. Iwasaki, L. Favergeon, N. Koga, Revealing the effect of water vapor pressure on the kinetics of thermal decomposition of magnesium hydroxide, Phys. Chem. Chem. Phys. 22 (2020) 13637–13649, https://doi.org/10.1039/ DOCP00446D
- [27] D. Dollimore, The techniques and theory of thermal analysis applied to studies on inorganic materials with particular reference to dehydration and single oxide systems, Sel. Annu. Rev. Anal. Sci. 2 (1972) 1–81, https://doi.org/10.1039/ AS9720200001.
- [28] L.C. Sögütoglu, F. Birkelbach, A. Werner, H. Fischer, H. Huinink, O. Adan, Hydration of salts as a two-step process: water adsorption and hydrate formation, Thermochim. Acta 695 (2021), https://doi.org/10.1016/j.tca.2020.178819.
- [29] J.W. Mullin, Crystallization, Elsevier, 2001.
- [30] S. Vyazovkin, A.K. Burnham, J.M. Criado, L.A. Pérez-Maqueda, C. Popescu, N. Sbirrazzuoli, ICTAC Kinetics Committee recommendations for performing kinetic computations on thermal analysis data, Thermochim. Acta 520 (2011) 1–19, https://doi.org/10.1016/j.tca.2011.03.034.
- [31] N. Lyakhov, M. Maciejewski, A. Reller, Theoretical considerations on the temperature and pressure dependence of the kinetics of reversible thermal decomposition processes of solids, J. Solid State Chem. 58 (1985) 398–400.
- [32] M. Deutsch, F. Birkelbach, C. Knoll, M. Harasek, A. Werner, F. Winter, An extension of the NPK method to include the pressure dependency of solid state reactions, Thermochim. Acta 654 (2017) 168–178, https://doi.org/10.1016/j. tca.2017.05.019.
- [33] A. Fopah Lele, F. Kuznik, H.U. Rammelberg, T. Schmidt, W.K.L. Ruck, Thermal decomposition kinetic of salt hydrates for heat storage systems, Appl. Energy 154 (2015) 447–458, https://doi.org/10.1016/j.apenergy.2015.02.011.
- [34] P.D. Goodell, P.S. Rudman, Hydriding and dehydriding rates of the LaNi5-H system, J. Less Common Met. 89 (1983) 117–125, https://doi.org/10.1016/0022-5088(83)90255-2.
- [35] T. Hirata, T. Matsumoto, M. Amano, Y. Sasaki, Dehydriding reaction kinetics in the improved intermetallic Mg2Ni H system, J. Less Common Met. 89 (1983) 85–91, https://doi.org/10.1016/0022-5088(83)90252-7.
- [36] L. Belkbir, E. Joly, N. Gerard, A kinetic study of the LaNi4.9Alo.1-H2 system, J. Less Common Met. 81 (1981) 199–206, https://doi.org/10.1016/0022-5088(81) 90026-6.
- [37] Y. Yamamoto, L. Favergeon, N. Koga, Thermal dehydration of lithium sulfate monohydrate revisited with universal kinetic description over different temperatures and atmospheric water vapor pressures, J. Phys. Chem. C 124 (2020) 11960–11976, https://doi.org/10.1021/ACS.JPCC.0C02739.
- [38] W. Luo, K.J. Gross, A kinetics model of hydrogen absorption and desorption in Tidoped NaAlH4, J. Alloy. Compd. 385 (2004) 224–231, https://doi.org/10.1016/J. JALLCOM.2004.05.004.
- [39] L. Greenspan, Humidity fixed points of binary saturated aqueous solutions, J. Res. Natl. Bur. Stand. 82A (1976) 89–96.
- [40] M.A. Stanish, D.D. Perlmutter, Rate processes in cycling a reversible gas-solid reaction, AIChE J. 30 (1984) 56–62, https://doi.org/10.1002/aic.690300110.
- [41] L. Favergeon, M. Pijolat, Influence of water vapor pressure on the induction period during Li ₂SO₄·H₂O single crystals dehydration, Thermochim. Acta 521 (2011) 155–160, https://doi.org/10.1016/j.tca.2011.04.018.
- [42] L. Okhrimenko, L. Favergeon, K. Johannes, F. Kuznik, New kinetic model of the dehydration reaction of magnesium sulfate hexahydrate: application for heat storage, Thermochim. Acta 687 (2020), 178569, https://doi.org/10.1016/J. TCA.2020.178569.
- [43] M. Fukuda, L. Favergeon, N. Koga, Universal kinetic description for thermal decomposition of copper(II) hydroxide over different water vapor pressures, J. Phys. Chem. C 123 (2019) 20903–20915, https://doi.org/10.1021/ACS. JPCC.9B04704/ASSET/IMAGES/LARGE/JP9B04704, 0010.JPEG.
- [44] A.K. Galwey, Magnitudes of Arrhenius parameters for decomposition reactions of solids, Thermochim. Acta 242 (1994) 259–264, https://doi.org/10.1016/0040-6031(94)85030-5.